

X-ray detected infrared excess AGN in the *Chandra* deep fields: a moderate fraction of *Compton*-thick sources[★]

I. Georgantopoulos^{1,2}, E. Rovilos³, E. M. Xilouris², A. Comastri¹, and A. Akylas²

¹ INAF - Osservatorio Astronomico di Bologna, via Ranzani 1, 40127, Italy
e-mail: ig@astro.noa.gr

² Institute of Astronomy & Astrophysics, National Observatory of Athens, Palaia Penteli, 15236 Athens, Greece

³ Max Planck Institut für Extraterrestrische Physik, Garching bei München, Germany

Received 12 March 2010 / Accepted 13 July 2010

ABSTRACT

We examine the properties of the X-ray-detected infrared excess AGN or dust obscured galaxies (DOGs) in the *Chandra* deep fields (CDFs). We find 26 X-ray-detected sources that obey the $24\ \mu\text{m}$ to *R*-band flux ratio criterion $f_{24}/f_R > 1000$. These are at a median redshift of 2.3, while their IR luminosities are above $10^{12} L_{\odot}$. Their X-ray luminosities are all above a few times $10^{42}\ \text{erg s}^{-1}$ in the 2–10 keV band, which unambiguously argues that they host AGN. Nevertheless, their IR spectral energy distributions are split between AGN (Mrk231) and star-forming templates (Arp220). Our primary goal is to examine their individual X-ray spectra in order to assess whether this X-ray-detected DOG population contains heavily obscured or even *Compton*-thick sources. The X-ray spectroscopy reveals a mixed bag of objects. We find that four out of the 12 sources with adequate photon statistics and hence reliable X-ray spectra show evidence for a hard X-ray spectral index with $\Gamma \sim 1$ or harder, which is consistent with a *Compton*-thick spectrum. In total 12 out of the 26 DOGs show evidence for flat spectral indices. However, owing to the limited photon statistics we cannot distinguish whether they are flat because they are reflection-dominated or because they show moderate amounts of absorption. Seven DOGs show relatively steep spectra $\Gamma > 1.4$, indicative of low column densities. All the above suggests a fraction of *Compton*-thick sources that does not exceed 50%. The average X-ray spectrum of all 26 DOGs is hard ($\Gamma \sim 1.1$) or even harder ($\Gamma \sim 0.6$) when we exclude the brightest sources. These spectral indices agree with the stacked spectrum of X-ray-undetected sources ($\Gamma \approx 0.8$ in the CDFN). This could suggest (but not necessarily prove) that X-ray undetected DOGs, in a similar way as the X-ray-detected ones presented here, are hosting a moderate fraction of *Compton*-thick sources.

Key words. X-rays: general – X-rays: diffuse background – X-rays: galaxies – infrared: galaxies

1. Introduction

The hard X-rays (2–10 keV) possess the advantage that they can penetrate large amounts of interstellar gas and thus can detect AGN which would be missed in optical wavelengths (Brandt & Hasinger 2005). The *Chandra* mission has probed the X-ray Universe at unparalleled depth. The deep 2Ms observations in the *Chandra* deep field (CDF) North and South (Giacconi et al. 2002; Alexander et al. 2003; Luo et al. 2008) resolved 80–90% of the extragalactic X-ray light, the X-ray background, in the 2–10 keV band and revealed a sky density of about 5000 sources per square degree down to a flux of $1 \times 10^{-16}\ \text{erg cm}^{-2}\ \text{s}^{-1}$ (Bauer et al. 2004). These deep CDF observations in combination with shallower *Chandra* and XMM surveys (e.g. COSMOS, Hasinger et al. 2007; AEGIS, Nandra et al. 2007) have provided us with the opportunity of studying with unprecedented accuracy the accretion history of the Universe (Ueda et al. 2003; LaFranca et al. 2005; Barger et al. 2005; Silverman et al. 2008; Brusa et al. 2009a; Aird et al. 2010).

However, even the extremely efficient X-ray surveys may be missing a fraction of heavily obscured sources. This is because at very high obscuring column densities ($>10^{24}\ \text{cm}^{-2}$) around the nucleus even the hard X-rays (2–10 keV) are significantly suppressed. These are the so-called *Compton*-thick

AGN (see Comastri 2004, for a review), where the probability for Thomson scattering becomes significant. The X-ray background synthesis models (Comastri et al. 1995; Gilli et al. 2007) can explain the peak of the X-ray background between 20–30 keV, where most of its energy density lies (e.g. Frontera et al. 2007; Churazov et al. 2007; Moretti et al. 2009) only by invoking a numerous population of *Compton*-thick sources. Nevertheless, the exact surface density of *Compton*-thick AGN required is still debatable (see e.g. Sazonov et al. 2007; Treister et al. 2009a). Additional evidence for an appreciable *Compton*-thick population comes from the directly measured space density of black holes in the local Universe. It is found that this space density is a factor of 1.5–2 higher than that predicted from the X-ray luminosity function (Marconi et al. 2004; Merloni & Heinz 2008), although the exact number depends on the assumed efficiency in the conversion of gravitational energy to radiation. This immediately suggests that the X-ray luminosity function is missing a large number of AGN. According to the X-ray background models a small number of *Compton*-thick AGN should be lurking among the faint sources in the CDFs. Because *Compton*-thick sources have a quite distinctive X-ray spectrum in the 2–10 keV band, i.e. either a spectral turnover in the transmission-dominated case or a flat continuum in the reflection-dominated case, X-ray spectroscopy provides a reasonably robust way for identifying these heavily obscured sources. Tozzi et al. (2006) and

[★] Figure 8 is only available in electronic form at <http://www.aanda.org>

Georgantopoulos et al. (2007, 2009) have looked for these directly in the CDFs with X-ray spectroscopy.

The advent of the IR *Spitzer* mission brought an additional perspective for the study of *Compton*-thick sources. This is because the absorbed optical and UV radiation heats the dust and is re-emitted at IR wavelengths. This implies that *Compton*-thick sources should emit copious amounts of mid-IR radiation. In particular, methods that combine the use of mid-IR and optical photometry have been quite fruitful. For example, the method proposed by Daddi et al. (2007) involves the selection of UV sources with mid-IR excess. Martinez-Sansigre et al. (2005) argue that a population of bright $24\ \mu\text{m}$ AGN with no $3.6\ \mu\text{m}$ detections is as numerous as unobscured QSOs at high redshift $z > 2$. Along these lines, Houck et al. (2005) have detected a population of $24\ \mu\text{m}$ bright sources that are very faint in the *R*-band and have $f_{24\ \mu\text{m}}/f_R > 1000$. Dey et al. (2008) and Pope et al. (2008) argue that these sources are associated with dust obscured galaxies (DOG) at high redshift ($z \approx 2$ with a small scatter $\sigma_z = 0.5$). At these distances the implied total IR luminosities are $L_{\text{IR}} > 10^{12-14} L_{\odot}$ which is comparable or in excess of low redshift ultra-luminous-infrared galaxies, ULIRG (Mirabel & Sanders 1996). Theoretical simulations prove that DOGs represent extreme gas-rich mergers in massive halos with $\sim 10^{13} M_{\odot}$ (Narayanan et al. 2010). Hereafter, we will adopt the notation DOGs for mid-IR bright optically faint sources. Fiore et al. (2008) argue that most DOGs may be associated with heavily obscured sources *below the flux limit* of the 1 Ms CDF-S survey. The stacked X-ray signal of the undetected DOGs in X-ray surveys, appears to be flat, which is indicative of absorbed sources, see Fiore et al. (2008), Georgantopoulos et al. (2008), Fiore et al. (2009), Treister et al. (2009b), Eckart et al. (2010), Donley et al. (2010). In particular, Fiore et al. (2009) argue that the content of *Compton*-thick sources among DOGs brighter than 550 mJy at $24\ \mu\text{m}$ may be as high as 90%. Fiore et al. (2009) point out that the bright mid-IR luminosities have been selected to ensure that any undetected X-ray source should have a very low $L_X/L_{24\ \mu\text{m}}$ ratio because it is either a *Compton*-thick AGN or a galaxy. Georgantopoulos et al. (2008) note that although it is possible that a significant number of *Compton*-thick sources lie among the X-ray-undetected DOGs, in the *Chandra* deep fields it is also likely that low-luminosity AGN with moderate absorption may mimic a flat spectrum. Finally, Pope et al. (2008) caution, on the basis of *Spitzer* IRS spectroscopy, that the normal galaxy (non-AGN) content of DOG samples may still be significant. In any case, it is impossible to argue unambiguously that these sources are *Compton*-thick, given that only a stacked hardness ratio is available and not individual good quality X-ray spectra.

Here, we attempt instead to address this issue by focusing on the DOGs which are present among the *detected* sources in deep X-ray surveys. We examine their X-ray spectra as well as their mid-IR properties and compare them with the properties of non-X-ray-detected DOGs. The primary aim is to examine whether there is evidence for *Compton*-thick or at least heavily obscured sources among the X-ray DOGs. We adopt $H_0 = 75\ \text{km s}^{-1} \text{Mpc}^{-1}$, $\Omega_M = 0.3$, $\Omega_{\Lambda} = 0.7$ throughout the paper.

2. Data

2.1. X-ray data

2.1.1. CDF-N

The CDF-N is centred at $\alpha = 12^{\text{h}}36^{\text{m}}49^{\text{s}}.4$, $\delta = +62^{\circ}12'58''$ (J2000). The 2Ms *Chandra* survey of the CDF-N consists of

20 individual ACIS-I (Advanced CCD Imaging Spectrometer) pointings observed between 1999 and 2002. The combined observations cover a total area of $447.8\ \text{arcmin}^2$ and provide the deepest X-ray sample currently available together with the *Chandra* deep field South (CDF-S) (Luo et al. 2008). Here, we use the X-ray source catalogue of Alexander et al. (2003), which consists of 503 sources detected in at least one of the seven X-ray spectral bands defined by these authors in the range 0.3–10 keV. The flux limit in the 2–10 keV band is $1.4 \times 10^{-16}\ \text{erg cm}^{-2}\ \text{s}^{-1}$. The Galactic column density towards the CDF-N is $1.6 \times 10^{20}\ \text{cm}^{-2}$ (Dickey & Lockman 1990).

2.1.2. CDF-S

The 2Ms CDF-S observations consist of 23 pointings. The first 1Ms (11 observations) was observed between 1999 and 2000. The analysis of the 1Ms data is presented in Giacconi et al. (2002) and Alexander et al. (2003). The analysis of all 23 observations is presented in Luo et al. (2008). The average aim point is $\alpha = 03^{\text{h}}32^{\text{m}}28^{\text{s}}.8$, $\delta = -27^{\circ}48'23''$ (J2000). The 23 observations cover an area of $435.6\ \text{arcmin}^2$ while 462 X-ray sources have been detected by Luo et al. (2008). The CDF-S survey reaches a sensitivity limit of $1.3 \times 10^{-16}\ \text{erg cm}^{-2}\ \text{s}^{-1}$ in the hard 2–8 keV band. The Galactic column density towards the CDF-S is $0.9 \times 10^{20}\ \text{cm}^{-2}$ (Dickey & Lockman 1990).

2.2. Spitzer

The central regions of both the CDF-N and the CDF-S have been observed in the mid-IR by the *Spitzer* mission (Werner 2000) as part of the Great Observatory Origin Deep Survey (GOODS). These observations cover areas of about $10 \times 16.5\ \text{arcmin}^2$ in both fields using the IRAC (3.6, 4.5, 5.8 and $8.0\ \mu\text{m}$) and the MIPS ($24\ \mu\text{m}$) instruments onboard *Spitzer*. Typical sensitivities for both surveys are $0.3\ \mu\text{Jy}$ and $80\ \mu\text{Jy}$ for the $3.6\ \mu\text{m}$ IRAC and $24\ \mu\text{m}$ MIPS respectively. The data products are available from the *Spitzer* data centre (<http://data.spitzer.caltech.edu/popular/goods/>).

3. Optical data

Both GOODS-North and GOODS-South have been imaged with ground-based telescopes as well as the *HST*. The *HST* observations are part of the GOODS Legacy survey and are described in detail in Giavalisco et al. (2004). The area imaged covers $2 \times 180\ \text{arcmin}^2$ with four ACS filters (*F435W*, *F606W*, *F775W*, and *F850LP*). The typical sensitivity is 27.8 mag(AB) in the *F850LP* filter. From the ground, an area larger than the GOODS-North has been imaged with the KPNO-4 m-MOSAIC and the Subaru-Suprime camera Capak et al. (2004) in the *U*, *B*, *V*, *R*, *I*, and *z'* bands. The catalogue contains sources detected in the *R* band with a limiting magnitude of 26.5(AB). The GOODS-South has been imaged with the CTIO-4 m-MOSAIC II camera as part of the MUSYC project Gawiser et al. (2006). The survey is complete to a total magnitude of $R = 25(\text{AB})$.

4. Sample definition

We use the “likelihood ratio” method of Sutherland & Saunders (1992) to cross-correlate the positions of the sources in different catalogues. For the northern field we follow the procedure described in detail in Rovilos et al. (2010). In short, we first find infrared (IRAC- $3.6\ \mu\text{m}$) counterparts to the X-ray

Table 1. X-ray, optical, and infrared fluxes of the DOG sample.

ID	RA (X-rays)	Dec (X-rays)	$f_{0.5-10\text{keV}}$	R	$3.6\ \mu\text{m}$	$f_{24\ \mu\text{m}}$
CDFN-92	189.0493	62.1707	2.50	25.967	17.834	160.6
CDFN-129	189.0914	62.2677	1.22	>26.500	18.542	104.6
CDFN-140	189.0986	62.1691	0.55	>26.500	18.820	148.2
CDFN-167	189.1302	62.1659	0.21	>26.500	18.732	196.0
CDFN-190	189.1483	62.2400	2.52	23.790	16.610	1426.0
CDFN-220	189.1755	62.2254	0.28	>26.500	18.981	204.8
CDFN-299	189.2413	62.3579	5.44	>26.500	18.077	199.1
CDFN-302	189.2448	62.2498	0.12	>26.500	19.001	117.4
CDFN-307	189.2472	62.3092	0.88	>26.500	18.815	271.0
CDFN-317	189.2568	62.1962	0.09	>26.500	16.806	664.4
CDFN-417	189.3563	62.2854	0.74	>26.500	18.380	172.6
CDFN-423	189.3605	62.3408	1.40	25.159	17.394	909.5
CDFS-95	53.0349	-27.6796	4.29	25.586	<25.986	241.0
CDFS-117	53.0491	-27.7745	2.47	26.366	22.047	110.0
CDFS-170	53.0720	-27.8189	0.13	26.704	21.692	83.4
CDFS-197	53.0916	-27.8532	0.59	26.116	22.547	238.0
CDFS-199	53.0923	-27.8032	0.52	>27.000	22.041	200.0
CDFS-230	53.1052	-27.8752	0.13	26.315	21.712	141.0
CDFS-232	53.1070	-27.7183	6.09	26.103	21.048	544.0
CDFS-293	53.1394	-27.8744	0.20	>27.000	22.959	351.0
CDFS-307	53.1467	-27.8883	2.51	>27.000	22.635	81.3
CDFS-309	53.1488	-27.8211	0.53	24.933	20.937	581.0
CDFS-321	53.1573	-27.8700	13.00	24.512	19.813	1080.0
CDFS-326	53.1597	-27.9313	0.81	26.759	21.353	177.0
CDFS-346	53.1703	-27.9297	7.26	24.582	21.528	717.0
CDFS-397	53.2049	-27.9180	2.11	27.009	21.155	163.0

Notes. The columns are: (1) Alexander ID number in the case of CDF-N or Luo ID in the case of CDF-S; (2) X-ray coordinates (J2000); (3) total 0.5–10 keV flux in units of 10^{-15} erg cm^{-2} s^{-1} ; (4) R -mag (AB) from Capak et al. (2004); (5) $3.6\ \mu\text{m}$ IRAC mag; (6) $24\ \mu\text{m}$ MIPS flux in μJy units.

sources, and then we search the optical catalogue of Capak et al. (2004) for optical identifications. *Spitzer*-MIPS counterparts are again pinned to $3.6\ \mu\text{m}$ positions. In order to select DOG candidates we search for sources with $\log(f_{24\ \mu\text{m}}/f_R) > 3$ defining $R = 26.5(\text{AB})$ as the lower limit for optical “non-detections” and find 19 candidates. We then inspect by eye the optical images of the “non-detections” (15/19) to check if there are any X-ray - IRAC sources with an obvious bright optical counterpart which is not listed in the Capak et al. (2004) catalogue. We find six such cases. We also remove source CDFN-109 from the list, because its MIPS counterpart is blended with a nearby source (CDFN-107) and the $24\ \mu\text{m}$ flux is not reliable. The final northern sample of DOGs is listed in Table 1.

In CDF-S, Grazian et al. (2006) provide the GOODS-MUSIC catalogue. This contains near-UV (U-band) magnitudes from the WFI at La Silla Arnouts et al. (2001) and VLT-VIMOS, optical magnitudes from the *HST*-ACS Giavalisco et al. (2004), near-infrared magnitudes ($J - H - K_S$) from VLT-ISAAC, and mid-infrared magnitudes from *Spitzer*-IRAC. The multi-band photometry has not been made by cross-correlating the various catalogues, but with implementing the “ConvPhot” algorithm of de Santis et al. (2007) to perform PSF-matching of the various images, and detecting the sources in the image with the best quality, in this case the ACS-F850LP.

We have used the Grazian et al. (2006) catalogue and cross-correlated it with the X-ray catalogue of Luo et al. (2008, 2010) using the maximum likelihood method, and also with the MUSYC catalogue to have a more complete coverage of the optical bands. The MUSYC catalogue contains sources detected in the combined $B - V - R$ band and the K_S band. We searched for *Spitzer*-MIPS counterparts to the optical sources and have selected the DOG candidates using the MUSYC R -band to compare with the $24\ \mu\text{m}$ flux. We found 22 candidate

sources assuming a lower limit of 27.0 mag(AB) for MUSYC non-detections. We again optically inspected the MUSYC images of the non-detections (11/21) for obvious bright optical counterparts not in the MUSYC catalogue and found eight such cases. The final southern sample of DOGs is listed in Table 1.

5. X-ray spectroscopy

The X-ray spectroscopy provides the most efficient tool for determining whether an AGN is absorbed. For moderate to heavy absorption ($<10^{24}$ cm^{-2}) the energy of the absorption cut-off gives an accurate measurement of the absorbing column density. On the other hand, the most heavily obscured sources, the *Compton*-thick AGN, can be identified mainly through the presence of a very flat spectrum with a photon-index of $\Gamma \sim 1$. This flat spectrum is the signature of a reflected continuum from obscuring material around the central source. Thanks to the long exposure times, the CDF observations yield a sufficient number of counts, allowing for X-ray spectroscopy to be performed in most cases.

We used the *SPEXTRACT* script in the CIAO v4.2 software package to extract spectra from the 20 individual CDF-N observations. The extraction radius varies between 2 and 4 arcsec with increasing off-axis angle. At low off-axis angles (<4 arcmin) this encircles 90% of the light at an energy of 1.5 keV. The same script extracts response and auxiliary files. The addition of the spectral response and auxiliary files has been performed with the FTOOL tasks *MATHPHA*, *ADDRMF* and *ADDRARF* respectively. We use the C-statistic technique (Cash 1979) which was specifically developed to extract spectral information from data with low signal-to-noise ratio. We use the XSPEC v12.5 software package for the spectral fits (Arnaud 1996).

5.1. Individual spectra

We fit the data using a power-law absorbed by a cold absorber. Where we have sufficient flux ($f_x > 1 \times 10^{-15}$ erg cm $^{-2}$ s $^{-1}$), we treat both the intrinsic column density and the photon index (Γ_1) as free parameters. Where we have limited photon statistics, we fix the power-law photon index to $\Gamma_1 = 1.8$ (Nandra & Pounds 1994; Tozzi et al. 2006), leaving only the column density as the free parameter. The results are shown in Table 2. As is customary in X-ray Astronomy, errors correspond to the 90% confidence level.

First, we investigate the brightest sources i.e. those 12 with a flux $f_x > 10^{-15}$ erg cm $^{-2}$ s $^{-1}$. There are four sources which prefer a very flat power-law index ($\Gamma_1 < 1$ at the 90% confidence level) instead of intrinsic absorption: 92, 190, 423 in CDF-N, and 346 in CDF-S. This flat spectrum is consistent with a reflection-dominated X-ray emission (e.g. Matt et al. 2004; Akylas & Georgantopoulos 2009) and therefore these sources can be considered as *Compton*-thick candidates. We present an example X-ray spectrum (CDFN-190) in Fig. 1. We note that the properties of CDFN-92 and CDFN-190 have been discussed in more detail in Georgantopoulos et al. (2009) as candidate *Compton*-thick sources. We discuss their findings particularly in respect with the presence of an FeK $_{\alpha}$ line. A high equivalent width (EW) FeK $_{\alpha}$ is often interpreted as the “smoking gun” giving away the presence of a *Compton*-thick AGN. CDFN-92 has an 90% upper limit of ≈ 0.7 keV (rest-frame). CDFN-190 which is associated with a sub-mm at a spectroscopic redshift of $z = 2.005$ (Chapman et al. 2005), has a detected FeK $_{\alpha}$ line with a rest-frame EW of ~ 0.7 keV. CDFN-423 had not been included in the sample of Georgantopoulos et al. (2009) because the source appeared to be very hard but with a large error on the photon index. The higher error probably had to do with the use of different fitting statistics (χ^2) in that paper in combination with the limited photon statistics ($f_{2-10} \approx 10^{-15}$ erg cm $^{-2}$ s $^{-1}$). No FeK $_{\alpha}$ line is detected in the spectrum of CDFN-423 with the 90% upper limit on the rest-frame EW being 0.65 keV. Finally, no FeK $_{\alpha}$ line is detected in the spectrum of CDFS-346 at rest-frame energy of 6.4 keV (360 eV upper limit). The four flat spectrum sources constitute an appreciable fraction (30%) of the sources with good quality X-ray spectra. We show the rest-frame column density distribution of these bright sources in Fig. 2 (excluding CDFS-95, for which there is no redshift). We count all four flat-spectrum sources as *Compton*-thick sources and therefore assign a value of $N_H = 10^{24}$ cm $^{-2}$ for these at the observer’s frame. For simplicity, we consider all column density upper limits as unabsorbed sources, assigning $N_H < 10^{22}$ cm $^{-2}$. Moreover, we show the column density distribution for our full sample in Fig. 2 (lower-panel): 18 spectra have been considered excluding the four faintest sources, where a spectral fit is not feasible, as well as the four sources with no available redshift.

In addition, we fit all the spectra with the simplest possible model i.e. a power-law model without absorption. The photon index Γ_2 results are given again in Table 2. This exercise is quite useful in demonstrating the effects of spectral degeneracy. For example, CDFS-117 with a steep spectral index of $\Gamma_1 = 1.81$ and an observer’s-frame column density of only 0.43×10^{22} cm $^{-2}$ in the absorbed power-law model has a flat equivalent photon-index of $\Gamma_2 \sim 1.1$ (in the power-law model), which could have been interpreted as a characteristic of a reflection-dominated spectrum. In Fig. 3 we plot the photon index Γ_2 as a function of the total X-ray flux. We see that the DOGs span a wide range in both flux and photon index. Seven sources are relatively unabsorbed with $\Gamma_2 > 1.4$. A photon index of $\Gamma = 1.4$ corresponds to the

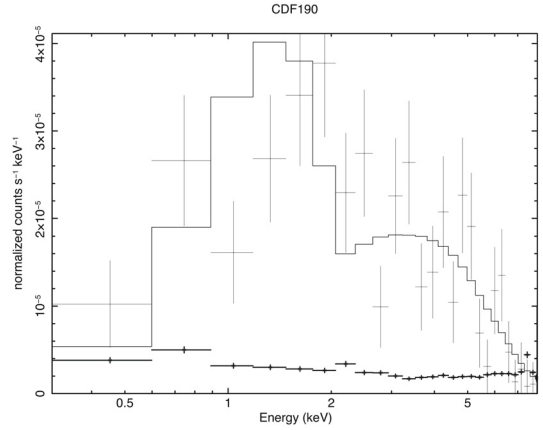


Fig. 1. Power-law fit to the spectrum of the source CDFN-190. The background is also plotted as thick crosses.

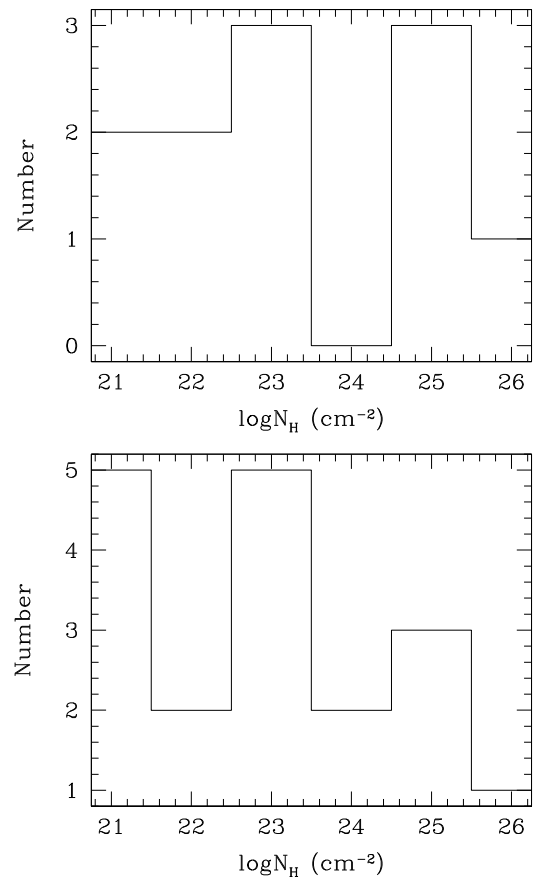


Fig. 2. *Upper panel:* rest-frame column density distribution of the brightest (11) sources with available redshift. *Lower panel:* rest-frame column density for all (18) sources with available redshift. Four sources with very low photon statistics have been excluded.

stacked (co-added) spectrum of all sources in the CDF-S (Tozzi et al. 2001). The above figure has to be interpreted with caution because of the effects of spectral degeneracy mentioned above. From this plot, we can securely tell which sources are relatively steep and thus unabsorbed, i.e. those with $\Gamma_2 > 1.4$. Thus we are confident that 7 out of 22 sources present little absorption. However, we cannot use this plot to find *Compton*-thick sources. This is because the flat Γ_2 sources could be hard because of an intrinsically flat spectral index suggestive of a reflection spectrum

Table 2. X-ray spectral fits.

ID (1)	z (2)	N_{H} (3)	Γ_1 (4)	Γ_2 (5)	L_x (6)
CDFN-92 [†]	0.95	<1	$-0.45^{+0.35}_{-0.40}$	$-0.50^{+0.34}_{-0.37}$	0.28
CDFN-129	2.33	<3.5	$0.29^{+1.27}_{-1.0}$	$-0.59^{+0.46}_{-0.51}$	4.8
CDFN-140	–	$0.8^{+0.5}_{-0.34}$	1.8	$0.59^{+0.37}_{-0.37}$	0.41
CDFN-167	–	$0.13^{+0.27}_{-0.13}$	1.8	$1.40^{+0.55}_{-0.52}$	0.46
CDFN-190 [†]	2.005	<0.04	$0.33^{+0.17}_{-0.21}$	$0.33^{+0.17}_{-0.21}$	1.28
CDFN-220	2.34	<0.4	1.8	$1.42^{+0.78}_{-0.65}$	0.3
CDFN-299	2.36	$0.12^{+0.04}_{-0.03}$	$1.74^{+0.20}_{-0.20}$	$1.43^{+0.11}_{-0.10}$	104.
CDFN-302	1.59	–	1.8	1.8	0.37
CDFN-307	–	$1.2^{+0.4}_{-0.4}$	1.8	$0.46^{+0.27}_{-0.44}$	1.39
CDFN-317	2.28	–	1.8	1.8	0.27
CDFN-417	1.90	<0.13	1.8	$1.73^{+0.25}_{-0.25}$	3.0
CDFN-423 [†]	2.07	<0.16	$0.48^{+0.4}_{-0.4}$	$0.50^{+0.45}_{-0.40}$	12.0
CDFS-95	–	<0.80	$1.00^{+0.72}_{-0.74}$	$0.51^{+0.36}_{-0.39}$	1.5
CDFS-117	2.24	$0.43^{+0.17}_{-0.20}$	$1.81^{+0.23}_{-0.34}$	$1.11^{+0.18}_{-0.16}$	2.56
CDFS-170	2.25	–	–	1.8	0.3
CDFS-197	2.57	$1.3^{+1.0}_{-0.60}$	1.8	$0.45^{+0.56}_{-0.61}$	0.4
CDFS-199	2.50	$0.77^{+0.70}_{-0.45}$	1.8	$0.47^{+0.51}_{-0.58}$	0.6
CDFS-230	2.73	–	–	1.8	0.7
CDFS-232	2.291	$0.62^{+0.16}_{-0.16}$	$1.77^{+0.13}_{-0.24}$	$0.87^{+0.12}_{-0.10}$	5.6
CDFS-293	3.62	$0.8^{+0.8}_{-0.4}$	1.8	$0.31^{+0.53}_{-0.43}$	1.4
CDFS-307	1.83	$1.0^{+0.5}_{-0.4}$	$1.67^{+0.26}_{-0.38}$	$0.58^{+0.17}_{-0.20}$	1.6
CDFS-309	2.57	$0.8^{+0.8}_{-0.6}$	1.8	$0.72^{+0.78}_{-0.72}$	0.4
CDFS-321	1.603	$0.2^{+0.04}_{-0.04}$	$2.2^{+0.12}_{-0.11}$	$1.64^{+0.06}_{-0.06}$	9.0
CDFS-326	2.50	<0.1	1.8	$1.76^{+0.46}_{-0.36}$	1.8
CDFS-346 [†]	3.06	$0.47^{+0.30}_{-0.30}$	$0.75^{+0.26}_{-0.34}$	$0.28^{+0.14}_{-0.17}$	4.8
CDFS-397	1.56	<0.07	$1.47^{+0.32}_{-0.19}$	$1.51^{+0.26}_{-0.22}$	1.2

Notes. The columns are: (1) X-ray ID as in Table 1 (2) redshift; three and two decimal numbers refer to spectroscopic and photometric redshift respectively; (3) intrinsic *Observer-frame* column density in units of 10^{22} cm⁻² for the power-law+absorption model; (4) photon index for the power-law+absorption model; (5) photon index for the power-law only model; Note that values with no error bars imply that the parameters have been fixed to this value. In four cases (CDFN-302, CDFN-317, CDFS-170 and CDFS-230) the very limited photon statistics did not allow even a single free parameter fit and therefore Γ_2 has been fixed to 1.8; (6) observed (uncorrected for absorption) luminosity in the 2–10 keV band in units of 10^{43} erg s⁻¹. Where there is no redshift available we assign the median redshift $z = 2.3$. [†] denotes candidate *Compton-thick* sources.

but possibly also because of merely moderate absorption. Only by examining sources which have adequate photon statistics and by leaving both the photon index and the column density as free parameters we can have some indication on whether a source is truly intrinsically flat. The inspection of the photon index Γ_2 column in Table 2 shows that there are 12 sources which appear flatter than $\Gamma < 1$. In this calculation we excluded sources CDFS-232 and CDFS-307 for which a fit with a moderate absorbing column is preferable.

5.2. Average X-ray spectrum

We derive the average X-ray spectrum of our sources separately for the CDF-N and CDF-S. The spectra are jointly fit with the photon index tied to a common value. We use the C-statistic in the spectral fits. The average spectra are fit in the 0.3–4 keV band. This band has been selected by Fiore et al. (2008) and Georgantopoulos et al. (2008) for the derivation of the stacked signal of non-X-ray detected DOGs in the CDF-S and CDF-N

respectively. Their choice was made mainly because at high energies the effective area rapidly decreases while the particle background becomes high. The best-fit results are shown in Table 3. The total number of counts in the spectra is given as well (source + background). Because the total spectrum may be dominated by the most bright source, we choose to present as well the best-fit results excluding the source which contains the most photon counts. In the CDF-N the co-added photon index is very hard ($\Gamma \approx 1.07$), while when we exclude the brightest source we obtain an even harder spectrum with $\Gamma \sim 0.6$. In the CDF-S the spectrum is comparable, with $\Gamma \approx 1.13$ and $\Gamma \sim 0.6$ when the brightest source is excluded. All photon indices above are significantly harder than $\Gamma \approx 1.4$, which corresponds to the co-added spectrum of all sources in the CDF-S (Tozzi et al. 2001) as well as to the spectrum of the X-ray background in the 2–10 keV band (De Luca & Molendi 2004).

We also derive the average spectrum separately for sources with power-law (AGN) SEDs and star-forming type SEDs (see next section for details). The results are given in Table 4. We see that there is no significant difference in the average X-ray

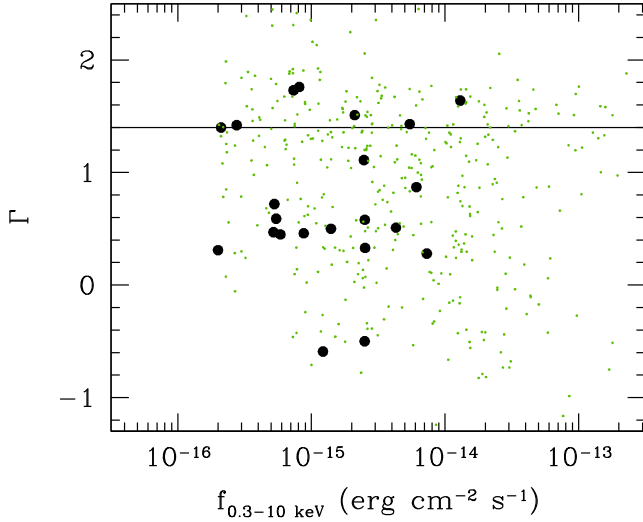


Fig. 3. Photon index Γ_2 of X-ray detected DOGs as a function of the total band flux (filled circles) for a column density fixed to $N_H = 0$. For comparison we plot the photon indices of all sources in the CDF-N (small dots).

Table 3. Average X-ray spectrum.

Sample	No	Counts	Γ (0.3–4 keV)
CDF-N	12	1831	1.07 ± 0.12
CDF-N (excl. #299)	11	1048	0.63 ± 0.17
CDF-S	14	4105	1.13 ± 0.06
CDF-S (excl. #321)	13	2121	0.65 ± 0.09

Table 4. Average X-ray spectrum according to IR SED.

Sample	No	Counts	Γ (0.3–4 keV)
Star-forming SED	19	2672	0.94 ± 0.08
Star-forming SED (excl. #299)	18	1889	0.58 ± 0.10
AGN SED	7	3264	1.22 ± 0.07
AGN SED (excl. #321)	6	1280	0.66 ± 0.11

spectrum of the two types of populations, at least when the brightest source is excluded.

6. Mid-IR properties

6.1. Mid-IR spectral energy distributions

We construct the spectral energy distribution (SED) to estimate the IR luminosities and also to get some idea about the dominant powering mechanism (AGN or star-formation) in the mid-IR part of the spectrum. We present the IRAC and MIPS $24 \mu\text{m}$ SED of the sources with available redshift in Fig. 7. For one source (CDFN-190) there are available sub-mm data (Chapman et al. 2005). We also overplot the best-matching SED template from Polletta et al. (2007). Polletta et al. (2006, 2007) have made extensive studies of the SEDs of X-ray selected AGN. Polletta et al. (2007) provide an inventory of template SEDs for various types of AGN and star-forming galaxies. In many cases the template of Mrk231 provides a satisfactory representation of the data which suggests an AGN underlying continuum. Mrk231 is the nearest broad-absorption-line QSO (Braitto et al. 2004) and

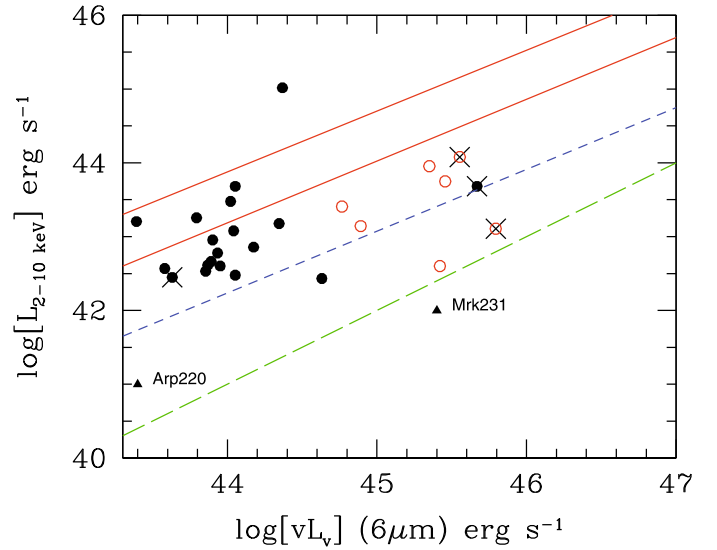


Fig. 4. 2–10 keV X-ray luminosity as a function of the $6 \mu\text{m}$ luminosity. The black (filled) and red (open) circles denote star-forming and AGN SEDs respectively. The solid lines denote the region occupied by unabsorbed AGN, while the region beyond the short-dashed line is populated by *Compton*-thick AGN in the local Universe (adapted from Bauer et al. 2010). The long-dashed line denotes the $L_X/L_{6 \mu\text{m}} \approx 10^{-3}$ luminosity ratio of the undetected DOGs in the CDF-N (from Georgakakis et al. 2010). The crosses denote the flat-spectrum sources (see text). Finally for comparison we plot the positions of Mrk231 and Arp220 in the diagram.

an ultra-luminous-infrared galaxy (ULIRG). The SED of the remaining sources is well represented by the Arp220 template. These are the sources with a distinct dip in their mid-IR spectra at a rest-frame wavelength below $10 \mu\text{m}$ Arp220 (e.g. Iwasawa et al. 2005) is a ULIRG whose far-IR SED is dominated by a very strong star-forming component. The IR luminosities are presented in Table 5. We emphasize that regardless of the mid-IR classification, most of our 26 DOGs can be classified almost certainly as AGN on the basis of their high X-ray luminosity and $L_X/L_{6 \mu\text{m}}$ diagram (see below). Their 2–10 keV X-ray luminosity (see Table 2) exceeds the $10^{42} \text{ erg s}^{-1}$ limit, which is considered to be the dividing line between star-forming galaxies and AGN (e.g. Zezas et al. 1998; Ranalli et al. 2003). Therefore the term “star-forming” mid-IR SED should not be misleading.

6.2. X-ray to $6 \mu\text{m}$ mid-IR luminosity ratio

One of the most reliable proxies of the intrinsic power of an AGN is the mid-IR luminosity (e.g. Lutz et al. 2004). The mid-IR emission is believed to provide a good measurement of the AGN luminosity even in the most obscured cases, since it is more extended than the X-ray absorbing material and thus represents an isotropic AGN property. Consequently we use the observed X-ray to mid-IR luminosity to provide more clues on whether our sources are obscured, expecting that the ratio of the X-ray to the mid-IR luminosity should be suppressed in the most obscured sources (e.g. Alexander et al. 2005, 2008). Here, we use the monochromatic $6 \mu\text{m}$ mid-IR luminosity instead of the full IR luminosity. This is because the former is more representative of the hot dust emission ($>300 \text{ K}$) and thus provides a better diagnostic of the AGN power. The $6 \mu\text{m}$ luminosity is derived from our SED fitting.

Table 5. Infrared luminosities.

ID ¹	L_{IR}^2	$\nu L_{\nu}(6 \mu\text{m})^3$	$\log(L_{2-10}/L_{6 \mu\text{m}})^4$	Template ⁵
CDFN-92 [†]	2.2	0.11	-1.19	1
CDFN-129	6.0	0.29	-0.69	1
CDFN-140	3.0	0.15	-1.26	1
CDFN-167	4.2	0.2	-1.2	1
CDFN-190 [†]	8.4	16.	-2.69	2
CDFN-220	6.0	0.29	-1.58	1
CDFN-299	12.	0.6	0.63	1
CDFN-302	2.0	0.1	-1.02	1
CDFN-307	1.1	2.0	-1.75	2
CDFN-317	23.	1.1	-2.21	1
CDFN-417	5.6	0.27	-0.55	1
CDFN-423 [†]	4.9	9.2	-1.49	2
CDFS-95	11.7	0.57	-1.18	1
CDFS-117	0.8	1.51	-1.36	2
CDFS-170	3.8	0.18	-1.33	1
CDFS-197	4.75	0.23	-1.36	1
CDFS-199	4.53	0.22	-1.16	1
CDFS-230	7.8	0.38	-1.33	1
CDFS-232	3.9	0.73	-1.71	2
CDFS-293	4.2	0.20	-0.96	1
CDFS-307	1.29	0.06	-0.20	1
CDFS-309	3.6	6.77	-2.82	2
CDFS-321	3.1	5.7	-1.41	2
CDFS-326	3.26	0.16	-0.55	1
CDFS-346 [†]	0.64	12.	-2.0	1
CDFS-397	5.6	0.28	-0.97	1

Notes. The columns are: (1) X-ray ID as in Table 1; (2) total (8–1000 μm) IR-luminosity in units of $10^{12} L_{\odot}$; (3) 6 μm νL_{ν} monochromatic luminosity in units of $10^{11} L_{\odot}$; (4) ratio of 2–10 keV X-ray to 6 μm monochromatic luminosity (where both luminosities in units erg s^{-1}); (5) template used from Polletta et al. (2007); 1 corresponds to Arp220 while 2 corresponds to Mrk231.

We present the monochromatic 6 μm IR luminosity against the 2–10 keV absorbed luminosity in Fig. 4. The area between the solid lines denotes the region of the X-ray to 6 μm plane where local AGN reside (Lutz et al. 2004). The area below the dashed line corresponds to low X-ray luminosity sources, i.e. *Compton*-thick sources (or alternatively normal galaxies). The crosses denote the sources with flat spectral index Γ . We see a relatively good correspondence between the flat- Γ sources and the low $L_x/L_{6 \mu\text{m}}$ sources. One of the lowest $L_x/L_{6 \mu\text{m}}$ sources is CDFN-190, a sub-mm galaxy with a spectroscopic redshift of $z = 2.005$ (Chapman et al. 2005). Other low $L_x/L_{6 \mu\text{m}}$ sources include CDFN-317 and CDFS-309. The first is among the two faintest sources in the CDF-N ($f_x \sim 1 \times 10^{-16} \text{ erg cm}^{-2} \text{ s}^{-1}$) where the very poor photon statistics did not even allow a single-parameter spectral fit ($L_x \approx 4 \times 10^{42} \text{ erg s}^{-1}$). The photon statistics of CDFS-309 allow a single parameter fit only. Its photon index is flat with $\Gamma_2 = 0.72^{+0.78}_{-0.72}$. Alternatively, assuming $\Gamma = 1.8$ its *rest-frame* column density would be $4 \times 10^{23} \text{ cm}^{-2}$.

6.3. IRAC colour-colour diagram

It is interesting to examine the position of our sources on the IRAC colour–colour diagram. Mid-IR colour selection has been suggested as a powerful tool for selecting AGN (see e.g. Martinez-Sansigre et al. 2005). The principle behind this approach is that luminous AGN have power-law spectral energy distribution in the mid-IR, while galaxies have characteristic blackbody spectra that peak at about 1.6 μm . The mid-IR colours of AGN are therefore redder than those of galaxies defining a characteristic wedge. Different combinations of mid-IR colours

have been proposed to select AGN (e.g. Lacy et al. 2004; Stern et al. 2005). The Stern et al. (2005) criteria are likely to suffer less contamination from normal galaxies, while at the same time they remain relatively sensitive to obscured AGN (but see Barmby et al. 2006; Cardamone et al. 2009). This method is graphically shown in Fig. 5. We see that all power-law SED fall within the wedge. However, there is also an appreciable number of DOGs that falls leftwards of the wedge close to the region of the parameter space occupied by Arp220 at high redshifts. The same trend has been observed for the X-ray undetected DOGs in the CDF-N (Georgantopoulos et al. 2008).

Pope et al. (2008) present IRS spectroscopy for a sample of 12 DOGs in the CDF-N. The spectroscopy shows that their sample is divided in half between AGN and star-forming galaxies. On the basis of their spectroscopic results these authors propose a colour diagram for the selection of AGN. They find that AGN-dominated sources separate very nicely at $S_{8.0 \mu\text{m}}/S_{4.5 \mu\text{m}} = 2$. We show this diagnostic diagram for our sources in Fig. 6. Interestingly most of our sources fall in the star-forming galaxy regime, although the vast majority are bona-fide AGN on the basis of their high X-ray luminosity and high $L_x/L_{6 \mu\text{m}}$ ratio. Brusa et al. (2009b) reach similar conclusions by examining the *Spitzer* colours of obscured AGN in the 1Ms CDFS observation.

6.4. Optical properties

In Fig. 8 we plot optical cutouts of the DOGs. The optical images are the combined $B_{435}\text{-}V_{606}\text{-}I_{775}\text{-}z_{850}$ frames from the *HST*-ACS survey in order to increase the signal-to-noise ratio. For CDF-S sources there are *HST* detections for all the sources in Grazian et al. (2006). In the north we are able to retrieve only

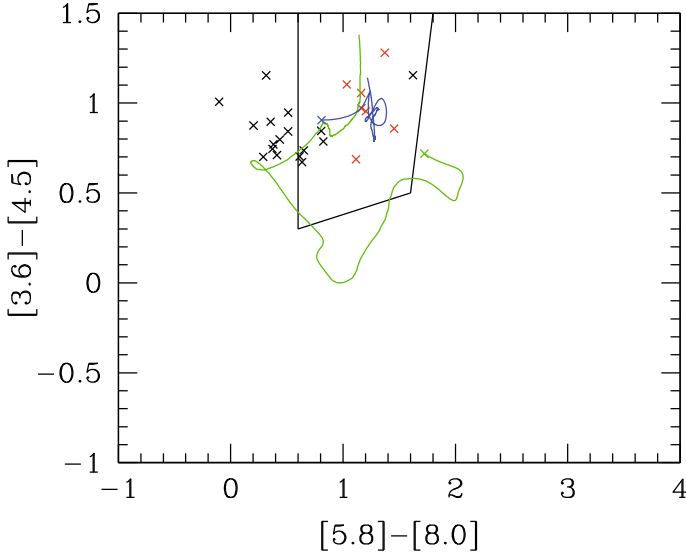


Fig. 5. Mid-IR colour-colour plot. Black and red crosses correspond to star-forming and AGN SEDs respectively. The wedge defines the AGN region following the selection criteria of Stern et al. (2005). The colour tracks define two different template SEDs as a function of redshift up to $z = 3$. The blue line represents the Mrk231 (ULIRG, *Compton-thick*) template, while the green line represents Arp220 (ULIRG, star-forming) SED. For each template the position of the redshift $z = 0$ is marked with a large cross. The templates are taken from Polletta et al. (2007).

10/12 sources because there are no *HST* counterparts for CDFN-140 and CDFN-307 in Giavalisco et al. (2004). In Table 6 we give the *HST* counterparts for the X-ray sources. For the detected sources we are able to inspect the morphology for many of them (typically when $z_{850} < 26.5$). The sources for which we are able to check the morphology are core-dominated but there is a circumnuclear structure for many of them ($\sim 2/3$).

The morphologies of the X-ray-detected DOGs are qualitatively in line with those of the overall DOG population. Melbourne et al. (2009) study with Keck adaptive optics the near-IR images of 15 DOGs. They find a correlation between the galaxy concentration and mid-IR luminosity in the sense that the most luminous DOGs exhibit higher concentration and smaller physical size. Bussmann et al. (2009a) present *HST* images of 31 DOGs. All but one of their DOGs (which follow AGN mid-IR SEDs) present spatially extended emission, but 90% also show significant unresolved components.

7. Discussion

7.1. Overall properties

We investigate the properties of 26 X-ray-detected DOGs in the CDF-N and CDF-S. Their redshifts (at least for the 22 DOGs for which there are available spectroscopic or photometric redshifts available) strongly cluster around $z \sim 2.3$. Although the uncertainties are admittedly high, because only four objects have an available spectroscopic redshift, this finding agrees well with the results of Pope et al. (2008) and Dey et al. (2008). Dey et al. (2008) measure spectroscopic redshifts for 86 DOGs in the Bootes field, finding a redshift distribution centred at $z = 1.99$. Pope et al. (2008) present mid-IR spectroscopy for a sample of 12 (out of 79) Spitzer-selected DOGs in GOODS-N, finding that the spectra lie in a tight distribution around $z \sim 2$. We find that

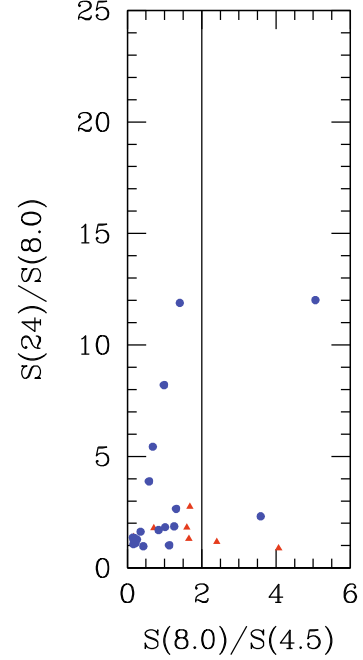


Fig. 6. Spitzer colour-colour diagram proposed to separate star-forming from AGN dominated DOGs. Circles (blue) and triangles (red) represent the DOGs in our sample with star-forming and AGN SEDs respectively. The solid line denotes the dividing line between AGN and star-forming galaxies at $S_{8.0}/S_{4.5} = 2$.

all our sources have $L_{\text{IR}} > 10^{12} L_{\odot}$ and thus are classified as ULIRGs. The uncertainties in the estimations of the total IR luminosities based on only IRAC and MIPS data are expected to be within a factor of 3 (see Dey et al. 2008; Bussmann et al. 2009b). This is because there are no far-IR or sub-mm measurements available (apart from one source) and thus the amount of cold dust available in these systems is uncertain. Bussmann et al. (2009b) estimate IR-luminosities $2 \times 10^{13} L_{\odot}$, higher than other classes of dusty $z \sim 2$ galaxy populations such as sub-mm galaxies, using SHARC-II 350 μm imaging of 12 DOGs in the Bootes field.

The vast majority of our sources are most probably hosting an AGN owing to the high X-ray luminosities ($L_{2-10} > 3 \times 10^{42} \text{ erg s}^{-1}$) and high $L_X/L_{6 \mu\text{m}}$ luminosity ratios (with the possible exception of the sources CDFN-317 and CDFS-309 see the discussion in Sect. 6.2). However, the mid-IR SEDs fail to reveal the presence of an AGN in many cases, suggesting that the AGN does not dominate the IR bolometric output. Only seven sources follow a power-law flux distribution that is suggestive of a broad range of warm dust temperatures similar to that observed in AGN dominated sources. The Mrk231 ULIRG template provides a good representation of these SEDs. Bussmann et al. (2009b) also find the same for their DOGs with sub-mm observations. The majority of our sources show a bump in their flux distribution, which is suggestive of a stellar continuum peaking at rest-frame wavelength of $1.6 \mu\text{m}$. These SEDs are well represented by the Arp220 ULIRG template. The mixture of star-forming and AGN SEDs we observe in our X-ray-detected DOGs is quite similar to that observed by Dey et al. (2008) in their Spitzer-selected sample. We note that the mean luminosity of the sample of Dey et al. (2008) is $\log[\nu L_{\nu}(8 \mu\text{m})] = 12$ ($\sigma = 0.64$), while in our sample the luminosities are somewhat lower with $\log[\nu L_{\nu}(6 \mu\text{m})] = 12$ ($\sigma = 1$).

Table 6. HST counterparts.

ID ¹	HST ²	α^3	δ^3	z^4	Morphology ⁵
CDFN-92	3844	189.04884	62.170823	25.42	core+extended
CDFN-129	6339	189.09149	62.267672	27.84	
CDFN-140	–	–	–	–	
CDFN-167	8764	189.13037	62.166202	26.52	core+extended
CDFN-190	10 044	189.14828	62.240091	22.92	spiral
CDFN-220	12 070	189.17521	62.225481	25.97	core+extended
CDFN-299	17 100	189.24136	62.358056	27.18	
CDFN-302	17 341	189.24465	62.249813	27.54	core
CDFN-307	–	–	–	–	
CDFN-317	18 291	189.25665	62.196300	27.28	
CDFN-417	25 122	189.35646	62.285470	25.56	core
CDFN-423	25 391	189.36045	62.340789	24.61	core+extended
CDFS-95	17 814	53.034100	–27.679634	25.25	core
CDFS-117	11 180	53.049049	–27.774496	25.08	core
CDFS-170	30 122	53.071991	–27.818924	26.27	
CDFS-197	30 202	53.091526	–27.853367	27.94	
CDFS-199	30 084	53.092266	–27.803137	26.21	core+extended
CDFS-230	30 199	53.105221	–27.875071	27.14	extended?
CDFS-232	15 260	53.107006	–27.718241	25.02	core+extended
CDFS-293	30 184	53.139332	–27.874464	27.93	
CDFS-307	2818	53.146698	–27.888338	26.06	core
CDFS-309	7814	53.148827	–27.821100	24.88	core+extended
CDFS-321	4119	53.157345	–27.870085	23.52	core
CDFS-326	461	53.159641	–27.931435	25.91	extended?
CDFS-346	540	53.170151	–27.929647	25.37	core+extended
CDFS-397	1059	53.204872	–27.917955	24.96	core+extended

Notes. The columns are: (1) X-ray ID as in Table 1; (2) HST ID from the catalogue of Giavalisco et al. (2004) and Grazian et al. (2006) for the CDF-N and CDF-S respectively; (3) *HST* coordinates (J2000); (4) *z*-band AB magnitude (F850LP) (5) comment on morphology.

7.2. Comparison with other X-ray observations of DOGs

Lanzuisi et al. (2009) have recently performed an X-ray study of luminous DOGs ($F_{24\ \mu\text{m}}/F_R > 2000$ and $F_{24\ \mu\text{m}} > 1.3$ mJy) in the Spitzer Wide-Area Infrared Extragalactic (SWIRE) survey. An area of 6deg^2 out of the total 50deg^2 of the SWIRE survey has been surveyed by *XMM-Newton* or *Chandra*. Their sample includes 44 DOGs in the redshift range $0.7 < z < 2.5$, of which 23 are detected in X-rays. These DOGs appear to be highly absorbed with about 50% having a column density $N_{\text{H}} > 10^{23}\text{cm}^{-2}$, while one source is associated with a transmission-dominated *Compton*-thick QSO. In comparison, in our sample out of the 18 objects with available redshifts and in which we were able to perform spectral fits, 11 have $N_{\text{H}} > 10^{23}\text{cm}^{-2}$. It appears that although the SWIRE sample is much brighter (its median flux is $\sim 1 \times 10^{-13}\text{erg cm}^{-2}\text{s}^{-1}$), the fraction of highly absorbed sources ($> 10^{23}\text{cm}^{-2}$) is not very different compared to our sample. However, the fraction of candidate *Compton*-thick sources is substantially higher in our fainter sample.

Fiore et al. (2009) investigate the X-ray properties of bright $24\ \mu\text{m}$ sources in the COSMOS survey (Elvis et al. 2009). They select 73 DOGs of which 31 are detected in X-rays with a mean luminosity of $\log[L_{(2-10\text{keV})}] \approx 43.5$ at a mean redshift $z = 1.55$. The hardness ratio of these sources is 0.50 ± 0.34 in the 0.3–1.5 vs. 1.5–6 keV bands, corresponding to a photon index of $\Gamma \sim 0.5$. This hardness ratio is identical to that of the remaining 42 non-detected DOGs (0.53 ± 0.14). The spectrum of the COSMOS DOGs is harder but consistent within the errors with the derived average spectrum of the DOGs in our sample.

Georgakakis et al. (2010) follow a different approach for identifying DOGs. They identify lower (spectroscopic) redshift

$z \approx 1$ sources in the AEGIS and CDFN surveys, which are analogues to the distant DOG population at $z \sim 2$. That is, their SED are similar to these of DOGs so, if placed at redshift of $z = 2$, they would classify as DOGs. They find nine such sources with X-ray counterparts. Their X-ray spectra are consistent with *Compton*-thin obscuration with only three sources presenting tentative evidence for *Compton*-thick obscuration. Ten more infrared-excess sources have no X-ray counterparts. Their SEDs are consistent with starburst activity showing no evidence for a hot dust component. Georgakakis et al. (2010) conclude that there is little evidence for the presence of a large fraction of luminous *Compton*-thick sources in either the X-ray-detected or undetected population of DOG analogues. As far as the X-ray detections are concerned, our findings are not that discrepant quantitatively, given that our fraction of *Compton*-thick sources is 4/12 among the brightest sources.

7.3. Comparison with X-ray-undetected DOGs

Fiore et al. (2008) examine the properties of DOGs in the CDF-S area which are undetected in the X-ray image. They find that the SEDs of most of these DOGs are dominated by AGN emission. The stacking analysis yields a hardness ratio corresponding to a flat spectral index of $\Gamma \sim 1$. They conclude that $80 \pm 15\%$ of these are likely to be highly obscured *Compton*-thick AGN. Georgantopoulos et al. (2008) have performed the same exercise in the CDF-N, finding a similar hardness ratio corresponding to a spectral index for the undetected DOG ($\Gamma \approx 0.8$). The average flux of the undetected DOGs in the CDF-N is $f_{2-10\text{keV}} \sim 6 \times 10^{-17}\text{erg cm}^{-2}\text{s}^{-1}$ (as compared to $f_{2-10\text{keV}} \sim 9 \times 10^{-16}\text{erg cm}^{-2}\text{s}^{-1}$ for those detected in this work). Fiore et al. (2009)

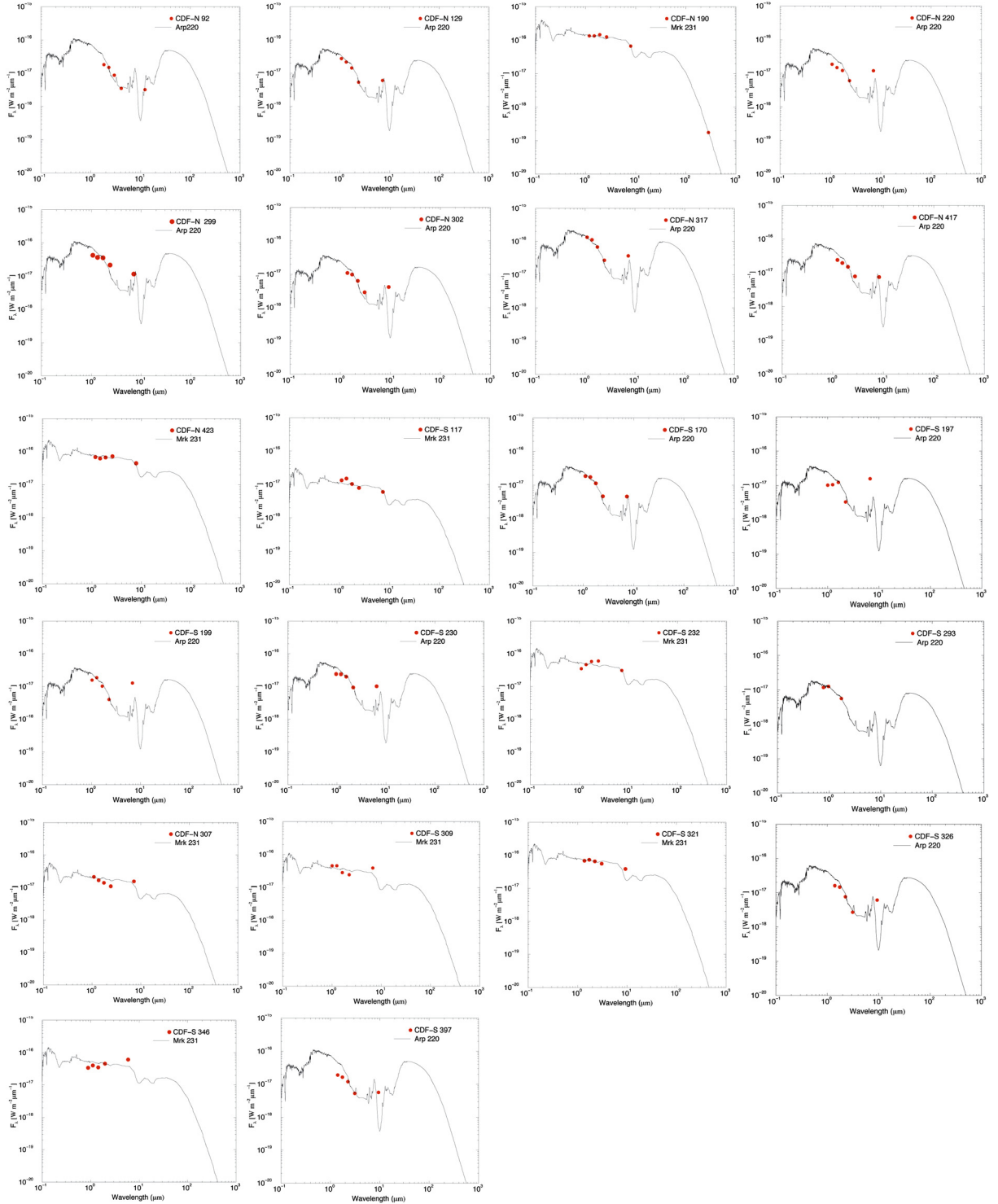


Fig. 7. IR spectral energy distributions.

look for X-ray undetected DOGs in the *Chandra*-COSMOS survey (Elvis et al. 2009). They claim that the number density of *Compton*-thick QSOs associated with DOGs is about half of all X-ray selected QSOs. Finally, Treister et al. (2009b) examine the properties of 211 heavily obscured AGN candidates in the extended CDF-S selecting objects with $f_{24\ \mu\text{m}}/f_R > 1000$ and $R - K > 4.5$. Eighteen sources are detected in X-rays with moderate column densities $\sim 10^{22-23}\ \text{cm}^{-2}$, while two of them appear to be *Compton*-thick. On the other hand, the undetected sources

show a hard average spectrum, which could be interpreted as a mixture of 90% *Compton*-thick objects and 10% star-forming galaxies. It should be kept in mind though that as only an average hardness ratio can be derived in the stacking analysis, one cannot definitively rule out the possibility that some of the sources are moderately absorbed ($\sim 10^{23}\ \text{cm}^{-2}$ at $z = 2$) instead of intrinsically flat. Our work here, which examines the individual X-ray spectra of the (albeit brighter) X-ray detected DOGs can provide an answer to this question. We find a mixed bag of objects.

At least four out of the 22 sources with derived spectra are good candidates for being reflection dominated *Compton*-thick sources. At most 12 sources could be intrinsically flat and thus *Compton*-thick candidates, but unfortunately the limited photon statistics do not allow us to distinguish between an intrinsically flat spectrum or a moderately absorbed one. At the same time a large number of DOGs present relatively steep spectra ($\Gamma > 1.4$) and thus are unambiguously associated with unabsorbed sources. One could argue that the X-ray detected DOGs are expected to be less absorbed compared to the undetected ones. This is simply because higher column densities diminish the X-ray flux and make the sources fainter than the CDF X-ray flux limit. Yet it is interesting that the detected DOGs have an X-ray spectrum very similar to the stacked spectrum of undetected DOGs ($\Gamma \sim 1$) or flatter. Because a significant number of the X-ray detected DOGs in the CDFs are showing moderate absorption, it is not unlikely that undetected DOGs follow a similar absorption pattern. Nevertheless, there is a significant difference between the X-ray detected and the undetected DOGs. The former have an X-ray to mid-IR luminosity ratio of $L_{2-10 \text{ keV}}/L_{6 \mu\text{m}} \approx -1.3$ (median), while the latter have $L_{2-10 \text{ keV}}/L_{6 \mu\text{m}} \approx -3$ (see Fig. 2 of Georgakakis et al. 2010). This could imply that the samples of undetected DOGs indeed contain a large fraction of *Compton*-thick sources. Then it is a mere coincidence that the average spectrum of the X-ray detected DOGs is comparable to that of undetected DOGs. Alternatively, there may be a substantial contamination of the X-ray undetected DOG samples from normal galaxies. Galaxies in the local Universe are known to have low X-ray to mid-IR luminosity ratios (Ranalli et al. 2003).

8. Summary

The mid-IR excess techniques have attracted much attention for claiming to be able to select *Compton*-thick AGN in a very efficient way. Here, we present a sample of 26 X-ray detected infrared-excess sources (DOGs) in the CDFs with $f_{24 \mu\text{m}}/f_R > 1000$. We examine their properties attempting to address the *Compton*-thick content of this sample mainly using X-ray spectroscopy. Our conclusions can be summarised as follows.

- We find that an appreciable fraction of the DOGs (7 out of 22) are associated with relatively unobscured sources, as they have $\Gamma > 1.4$. These are unobscured AGN rather than normal galaxies, as confirmed by their high X-ray luminosities.
- We identify a number of intrinsically flat $\Gamma < 1$ sources: 4 out of the 12 with good photon statistics. These could be associated with *Compton*-thick AGN. If we include the sources with poorer photon statistics, the amount of flat sources could be as many as 12 out of 26. In this respect we find that the infrared-excess techniques can indeed unveil a significant number of heavily obscured AGN at high redshifts.
- The fraction of *Compton*-thick sources could then vary roughly from 30% to 50%. This is clearly lower than that reported in previous studies of stacking analyses of X-ray-undetected DOG samples.
- The average spectrum of the X-ray detected DOGs is very similar if not harder than that of undetected DOGs in the CDFs.

Acknowledgements. We thank the referee Fabrizio Fiore for many useful comments and suggestions. I.G. and A.C. acknowledge the Marie Curie fellowship FP7-PEOPLE-IEF-2008 Prop. 235285. A.C. acknowledges receipt of ASI grants

I/023/05/00 and 1/88/06. We acknowledge the use of *Spitzer* data provided by the *Spitzer* Science Center. The *Chandra* data were taken from the *Chandra* Data Archive at the *Chandra* X-ray Center.

References

- Aird, J., Nandra, K., Laird, E. S., et al. 2010, MNRAS, 401, 2531
 Akylas, A., & Georgantopoulos, I. 2009, A&A, 500, 999
 Arnaud, K. A. 1996, Astronomical Data Analysis Software and Systems V, ed. Jacoby, G. & Barnes, J., ASP Conf. Ser., 101, 17
 Arnouts, S., Vandame, B., Benoist, C., et al. 2001, A&A, 379, 740
 Alexander, D. M., Bauer, F. E., Brandt, W. N., et al. 2003, AJ, 126, 539
 Alexander, D. M., Bauer, F. E., Chapman, S. C. et al. 2005, ApJ, 632, 736
 Alexander, D. M., Chary, R. R., Pope, A. et al. 2008, ApJ, 687, 835
 Barger, A. J., Cowie, L. L., Capak, P., et al. 2003, AJ, 126, 632
 Barger, A. J., Cowie, L. L., Mushotzky, R. F., et al. 2005, AJ, 129, 578
 Barmby, P., Alonso-Herrero, A., Donley, J. L. et al., ApJ, 2006, 642, 126
 Bauer, F. E., Alexander, D. M., Brandt, W. N., et al. 2004, AJ, 128, 2048
 Bauer, F. E., Yan, L., Sajina, A., & Alexander, D. M. 2010, ApJ, 710, 212
 Braito, V., Della Ceca, R., Piconcelli, E., et al. 2004, A&A, 420, 79
 Brandt W. N., & Hasinger, G. 2005, ARA&A, 43, 827
 Brusa, M., Comastri, A., Gilli, R., et al. 2009a, ApJ, 693, 8
 Brusa, M., Fiore, F., Santini, P., et al. 2009b, A&A, 507, 1277
 Bussmann, R. S., Dey, A., Lotz, J., et al. 2009a, ApJ, 693, 750
 Bussmann, R. S., Dey, A., Borys, C., et al. 2009b, ApJ, 705, 184
 Capak, P., Cowie, L. L., Hu, E. M., et al. 2004, AJ, 127, 180
 Cardamone, C. N., Urry, C. M., Damen, M., et al. 2008, ApJ, 680, 130
 Cash, W. 1979, ApJ, 228, 939
 Comastri, A. 2004, ASSL, 308, 245
 Comastri, A., Setti, G., Zamorani, G., & Hasinger, G. 1995, A&A, 296, 1
 Churazov, S. C., Blain, A. W., Smail, I., & Ivison, R. J. 2005, ApJ, 622, 772
 Churazov, E., Sunyaev, R., Revnivtsev, M., et al. 2007, A&A, 467, 529
 Daddi, E., Alexander, D. M., Dickinson, M. et al. 2007, ApJ, 670, 173
 De Luca, A., & Molendi, S. 2004, A&A, 419, 837
 de Santis, C., Grazian, A., Fontana, A., & Santini, P. 2007, NewA, 12, 271
 Dey, A., Soifer, B. T., Desai, V. et al. 2008, ApJ, 677, 943
 Dickey, J. M., & Lockman, F. J. 1990, ARA&A, 28, 215
 Dickinson, M., & Giavalisco, M., The Goods Team. 2003, in The Mass of Galaxies at Low and High Redshift, ed. R. Bender & A. Renzini (Springer-Verlag), 324
 Donley, J. L., Rieke, G. H., Alexander, D. M., et al. 2010, ApJ, 719, 1393
 Eckart, M. E., McGreer, I. D., Stern, D., Harrison, F. A., & Helfand, D. J. 2010, ApJ, 708, 584
 Elvis, M., Civano, F., Vignali, C., et al. 2009, ApJS, 184, 158
 Fiore, F., Grazian, A., Santini, P., et al. 2008, ApJ, 672, 94
 Fiore, F., Puccetti, S., Brusa, M. et al. 2009, ApJ, 693, 447
 Frontera, F., Orlandini, M., & Landi, R. 2007, ApJ, 666, 86
 Gawiser, E., van Dokkum, P. G., Herrera, D., et al. 2006, ApJS, 162, 1
 Georgakakis, A., Rowan-Robinson, M., Nandra, K., et al. 2010, MNRAS, 406, 420
 Georgantopoulos, I., Georgakakis, A., & Akylas, A. 2007, A&A, 466, 823
 Georgantopoulos, I., Georgakakis, A., Rowan-Robinson, M., & Rovilos, E. 2008, A&A, 484, 671
 Georgantopoulos, I., Akylas, A., Georgakakis, A., & Rowan-Robinson, M. 2009, A&A, 507, 747
 Giacconi, R., Zirm, A., Wang, J., et al. 2002, ApJS, 139, 369
 Giavalisco, M., Ferguson, H. C., Koekemoer, A. M., et al. 2004, ApJ, 600, 93
 Gilli, R., Comastri, A., & Hasinger, G. 2007, A&A, 463, 79
 Grazian, A., Fontana, A., de Santis, C., et al. 2006, A&A, 449, 951
 Houck, J. R., Soifer, B. T., & Weedman, D. 2005, ApJ, 622, L105
 Iwasawa, K., Sanders, D. B., Evans, A. S., et al. 2005, MNRAS, 357, 565
 Lacy, M., Storrie-S, Lombardi, L. J., et al. 2004, ApJS, 154, 166
 La Franca, F., Fiore, F., Comastri, A., et al. 2005, A&A, 435, 864
 Lanzuisi, G., Piconcelli, E., Fiore, F., et al. 2009, A&A, 498, 67
 Luo, B., Bauer, F. E., Brandt, W. N., et al. 2008, ApJS, 179, 19
 Luo, B., Brandt, W. N., Xue, Y. Q., et al. 2010, ApJS, 187, 560
 Lutz, D., Veilleux, S., & Genzel, R. 1999, ApJ, 517, L13
 Lutz, D., Maiolino, R., Spoon, H. W. W., & Moorwood, A. F. M. 2004, A&A, 418, 465
 Marconi, A., Risaliti, G., Gilli, R., et al. 2004, MNRAS, 351, 169
 Martinez-Sansigre, A., Rawlings, S., Lacy, M., et al. Nature, 436, 666
 Matt, G., Bianchi, S., Guainazzi, M., & Molendi, S. 2004, A&A, 421, 473
 Merloni, A., & Heinz, S. 2008, MNRAS, 388, 1011
 Mirabel, I. F., & Sanders, D. B. 1996, ARA&A, 34, 749
 Moretti, A., Pagani, C., Cusumano, G., et al. 2009, A&A, 493, 501
 Nandra, K., & Pounds, K. 1994, MNRAS, 268, 405
 Nandra, K., Georgakakis, A., Willmer, C. N. A., et al. 2007, ApJ, 660, L11

- Narayanan, D., Arjun, D., Hayward, C. C., et al. 2010, MNRAS, 407, 1701
Polletta, M., Wilkes, B. J., Siana, B., et al. 2006, ApJ, 642, 673
Polletta, M., Tajer, M., Maraschi, L., et al. 2007, ApJ, 663, 81
Pope, A., Bussmann, R. S., Dey, A., et al. 2008, ApJ, 689, 127
Ranalli, P., Comastri, A., & Setti, G. 2003, A&A, 399, 39
Rovilos, E., Georgantopoulos, I., & Akylas, A. 2010, A&A, 522, A11
Sazonov, S., Krivonos, R., Revnivtsev, M., Churazov, E., & Sunyaev, R. 2008, A&A, 482, 517
Silverman, J. D., Green, P. J., Barkhouse, W. A., et al. 2008, ApJ, 679, 118
Stern, D., Eisenhardt, P., & Gorjian, V. 2005, ApJ, 631, 163
Sutherland, W., & Saunders, W. 1992, MNRAS, 259, 413
Tozzi, P., Rosati, P., Nonino, M., et al. 2001, ApJ, 562, 42
Tozzi, P., Gilli, R., Mainieri, V., et al. 2006, A&A, 451, 457
Treister, E., Urry, C. M., & Virani, S. 2009a, ApJ, 696, 110
Treister, E., Cardamone, C. N., Schawinski, K., et al. 2009b, ApJ, 706, 535
Ueda, Y., Akiyama, M., Ohta, K., & Miyaji, T. 2003, ApJ, 598, 886
Werner, M. W. 2000, SPIE, 4131, 1
Zezas, A. L., Georgantopoulos, I., & Ward, M. J. 1998, MNRAS, 301, 915

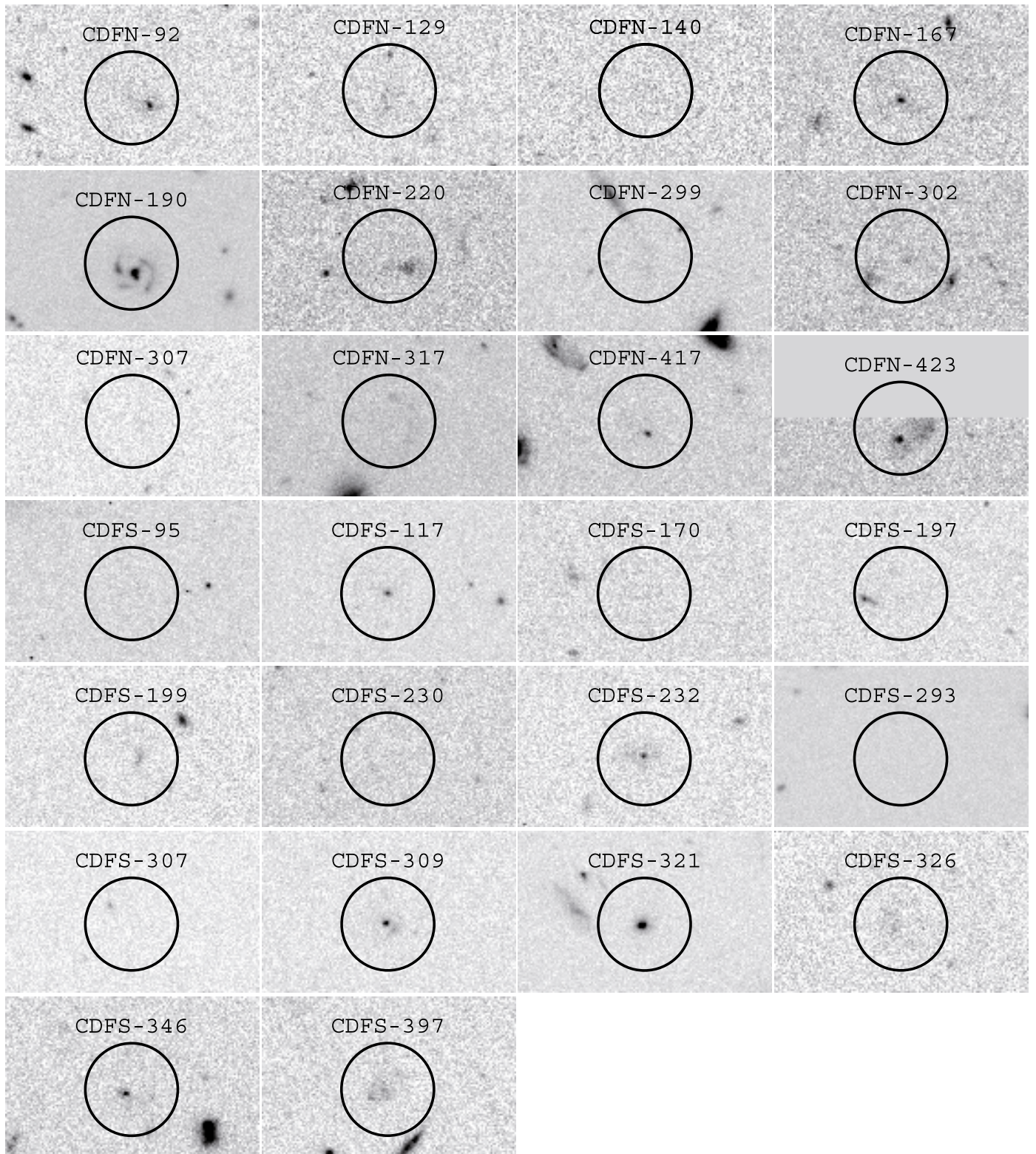


Fig. 8. Cutout images of the sources listed in Table 1. Ingreyscale we show the combined $B_{435}-V_{606}-I_{775}-z_{850}$ image from the *HST* survey. Circles mark the positions of the MIPS $24\ \mu\text{m}$ sources with $3''$ diameters. Note: all *HST* counterparts fall within the circle apart from CDFS-95 which is the bright source westwards.